phys. stat. sol. (a) **166**, 127 (1998)

Subject classification: 62.20.Fe; 61.72.Lk; S10.15

Plastic Deformation of Cubic Zirconia Single Crystals at 1400 °C

B. Baufeld[1]) , D. Baither[2]), M. Bartsch, and U. Messerschmidt[3])

Max Planck Institute of Microstructure Physics, Weinberg 2, D-06120 Halle/Saale, Germany
phone: +49-345-55 82-9 27; Fax: +49-345-5 51 12 23

(Received December 3, 1997)

Dedicated to Professor Dr. Manfred Rühle on the occasion of his 60th birthday

Cubic zirconia single crystals stabilized with 11 mol% yttria were deformed in air at 1400 °C and around 1200 °C at different strain rates along [1$\bar{1}$2] and [100] compression directions. The strain rate sensitivity of the flow stress was determined by strain rate cycling and stress relaxation tests. The microstructure of the deformed specimens was investigated by transmission high-voltage electron microscopy, inlcuding contrast extinction analysis for determining the Burgers vectors as well as stereo pairs and wide-angle tilting experiments to find the active slip planes. At deformation along [1$\bar{1}$2], the primary and secondary slip planes are of {100} type. Previous experiments had shown that the dislocations move easily on these planes in an athermal way. During deformation along [100], mainly dislocations on {110} planes are activated, which move in a viscous way by the aid of thermal activation. The discussion of the different deformation behaviours during deformation along [1$\bar{1}$2] and [100] is based on the different dynamic properties of dislocations and the fact that recovery is an essential feature of the deformation of cubic zirconia at 1400 °C. The results on the shape of the deformation curve and the strain rate sensitivity of the flow stress are partly at variance with those of previous authors.

1. Introduction

The plasticity of cubic zirconia single crystals has been investigated in some detail by several researchers. The first tests were performed at temperatures around 1400 °C [1 to 7]. Such high temperatures were chosen as it was believed that the brittle-to-ductile transition temperature is above 1000 °C [5]. Recently, cubic zirconia was successfully deformed in ambient atmosphere at lower temperatures down to 400 °C [8 to 11], and under confining hydrostatic pressure between 250 and 550 °C [12 to 14]. In addition to conventional compression experiments, *in situ* tensile straining tests were performed in a high-voltage transmission electron microscope (HVEM) at 1150 °C [9, 10, 15]. With the heating techniques improved it became possible to perform experiments also at higher temperatures up to 1800 °C [16, 17]. Most of the experiments were carried out with a [1$\bar{1}$2] compression axis to activate single slip on the (001) 1/2[1$\bar{1}$0] slip system.

---

[1]) Present address: Max Planck Institute of Metals Research, PML, Heisenbergstr. 5, D-70569 Stuttgart, Germany.

[2]) Present address: Max Planck Institute of Metals Research, Seestr. 92, D-70174 Stuttgart, Germany.

[3]) Corresponding author.

The results in the wide temperature range from 250 to 1800 °C suggest that different microprocesses control the deformation behaviour in different temperature ranges. While these processes are relatively well understood in the low temperature ranges [9, 10], there are a number of open questions in the most investigated range around 1400 °C. This concerns, e.g., the type of slip planes activated as secondary planes as well as the mechanism by which the yttria content influences the flow stress, which was originally interpreted as solution hardening [1]. However, no indications of this process were found at lower temperatures in the *in situ* experiments [9, 10, 15].

Therefore, more detailed compression tests were carried out at 1400 °C. The procedures were similar to those described in [7]. However, the experiments were performed in a wider range of strain rates between 10^{-6} and 10^{-4} 1/s and on samples with a [100] compression axis in addition to the usual $[1\bar{1}2]$ axis. The results of the compression tests were supplemented by a careful transmission electron microscopy (TEM) analysis of the dislocation structures in the deformed specimens. Moreover, some experiments were carried out at about 1200 °C in order to elucidate the transition of the deformation behaviour at 1400 °C to that at intermediate temperatures between about 900 and 1100 °C. The existing models of the plastic deformation of cubic zirconia at high temperatures are critically discussed on the basis of the new data.

2. Experimental

Rectangular samples of fully stabilized cubic zirconia single crystals[4]) were prepared to be $8 \times 2 \times 2$ mm^3 in size. The producer stated the concentration of stabilizing Y_2O_3 to be 9.4 mol%, whereas EDX proved 11 mol%. Most crystals were oriented for single slip on the (001) $1/2[1\bar{1}0]$ slip system, i.e. for compression in $[1\bar{1}2]$ direction with $(\bar{1}11)$ and (110) side faces. Some samples were prepared for compression in [100] direction with {001} side faces in order to suppress slip on cube planes. The specimens were cut with a wire saw and boron slurry, ground and polished using a 3 μm diamond suspension on brass and a polishing cloth, respectively.

The compression tests were performed in a single-screw testing machine[5]) equipped with a high-temperature furnace, push rods of Al_2O_3 and compression anvils of SiC, as schematically drawn in Fig. 1. Long touch rods of Al_2O_3 connected with a water-cooled linear variable differential transducer (LVDT) were used for the strain measurements. Thus, mainly the deformation of the sample itself is measured by the LVDT. The machine can be operated under closed loop strain control with an accuracy of 0.05 μm. Under these conditions, virtually the set-up is of high elastic stiffness, mainly that of the specimen, which allows one to measure stress relaxation curves over wide ranges of strain rate with little plastic strain being consumed. Most experiments were performed at 1400 °C in air. For comparison, some specimens were deformed at lower temperatures between 1100 and 1200 °C.

In the present work, the total strain ε_t and the stress σ are related to the initial length l_0 and cross section A of the specimens. The dependence of the flow stress on the plastic strain rate $\dot{\varepsilon}$ is described by the strain rate sensitivity

$$I = \Delta\sigma/\Delta \ln \dot{\varepsilon} \,, \tag{1}$$

[4]) Ceres Corp., Waltham, Mass.
[5]) Instron 8562.

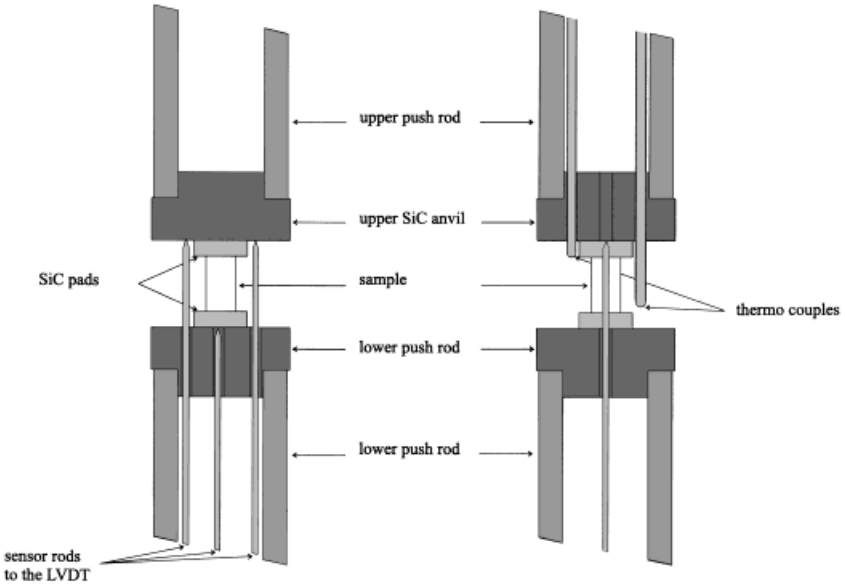

Fig. 1. Schematic drawing of the anvils with the sample in two viewing directions. a) View on the three touch-rods, which lead to the LVDT (left part), b) view on the thermoelements (right part)

or, using a power law $\dot{\varepsilon} \sim \sigma^{m^*}$, by the apparent stress exponent $m^* = \Delta \ln \dot{\varepsilon} / \Delta \ln \sigma$, which is related to I by

$$m^* = \sigma / I \,. \tag{2}$$

The strain rate sensitivity I is determined either from strain rate cycling (SRC) experiments, or from stress relaxation tests (R). Here, the plastic strain rate $\dot{\varepsilon}$ is proportional to the negative stress rate

$$\dot{\varepsilon} = -(CA/l_0)\, \dot{\sigma} \,. \tag{3}$$

C is the elastic compliance inside the gauge length of the LVDT. Consequently, in a plot of $\ln(-\dot{\sigma})$ versus σ of the relaxation data, the inverse slope $\Delta\sigma / \Delta \ln(-\dot{\sigma})$ is equal to the strain rate sensitivity I. In the following, this kind of plot will be called a relaxation curve. The apparent stress exponent m^* is the slope in a plot of $\ln(-\dot{\sigma})$ versus $\ln \sigma$. In the diagrams, the initial stress rate was calculated by eq. (3) from the strain rate before the relaxation tests (large symbols).

The dislocation structures created by the deformation were studied by TEM in a high-voltage electron microscope (HVEM). In order to detect possible changes of the microstructure formed during deformation, particularly during cooling, samples were cooled down either in the unloaded state, as it is usually done, or under full load applying the load-control mode. The cooling rate was limited to 12 K/min owing to the design of the equipment. The specimens were unloaded at 900 °C since, at 800 °C, a glass phase broke, which had formed at high temperature between the SiC anvils and the Al_2O_3 compression rods. This initiated strong vibrations resulting in specimen failure. It is believed that diffusion-controlled recovery processes do not change the dislocation structure below 900 °C.

The TEM specimens were prepared using standard procedures, with a $[\bar{1}11]$ foil normal for samples deformed along $[1\bar{1}2]$ and [001] for deformation along [100]. The HVEM was operated at an acceleration voltage of 1000 kV. It was not necessary to coat the samples despite the low electrical conductivity of zirconia.

3. Results of Deformation Experiments

3.1 Deformation along $[1\bar{1}2]$

The shape of the stress–strain curves of cubic zirconia deformed at 1400 °C along $[1\bar{1}2]$ essentially depends on the strain rate applied. As Fig. 2 shows, the stress–strain curves exhibit the same shape as in the early experiments [1 to 6], with an upper and lower yield point followed by zero work hardening, at strain rates below about 5×10^{-5} 1/s. At higher strain rates, however, the yield point disappears, with weak work hardening occurring ($\Theta = \mathrm{d}\sigma/\mathrm{d}\varepsilon \cong 1$ GPa). The behaviour is the same in experiments interrupted by stress relaxation or SRC tests, as demonstrated in Fig. 3.

At 1400 °C, not only the shape of the deformation curves but also the strain rate sensitivity I strongly depends on the basic strain rate. As Fig. 3a qualitatively demonstrates for a strain rate ratio of 5, at high strain rates and low strains the flow stress hardly changes during the SRC experiments, which corresponds to a very low strain rate sensitivity I. With increasing strain, the strain rate sensitivity increases. Respective results are summarized in Fig. 4a. At low strain rates, however, similar SRC experiments result in a large change of the flow stress which hardly depends on strain as shown in Fig. 3b. The corresponding strain rate sensitivities are plotted in Fig. 4b as a function of strain. The increase of the strain rate sensitivity I with increasing strain at high strain rates recovers during annealing. This is shown in the stress–strain curve of Fig. 5, where the sample was unloaded after the stress relaxation test R15, annealed for 40 min at

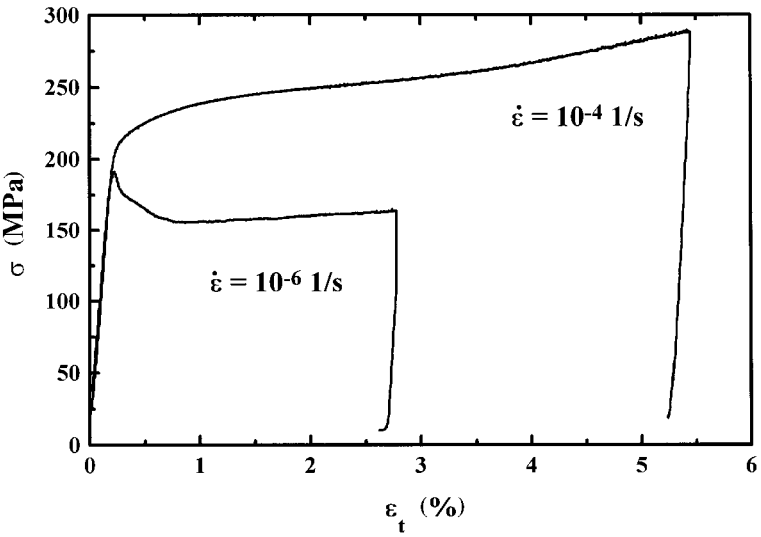

Fig. 2. Stress–strain curves of Y_2O_3-stabilized ZrO_2 single crystals deformed along $[1\bar{1}2]$ at 1400 °C with strain rates of $\dot{\varepsilon} = 10^{-6}$ and 10^{-4} 1/s

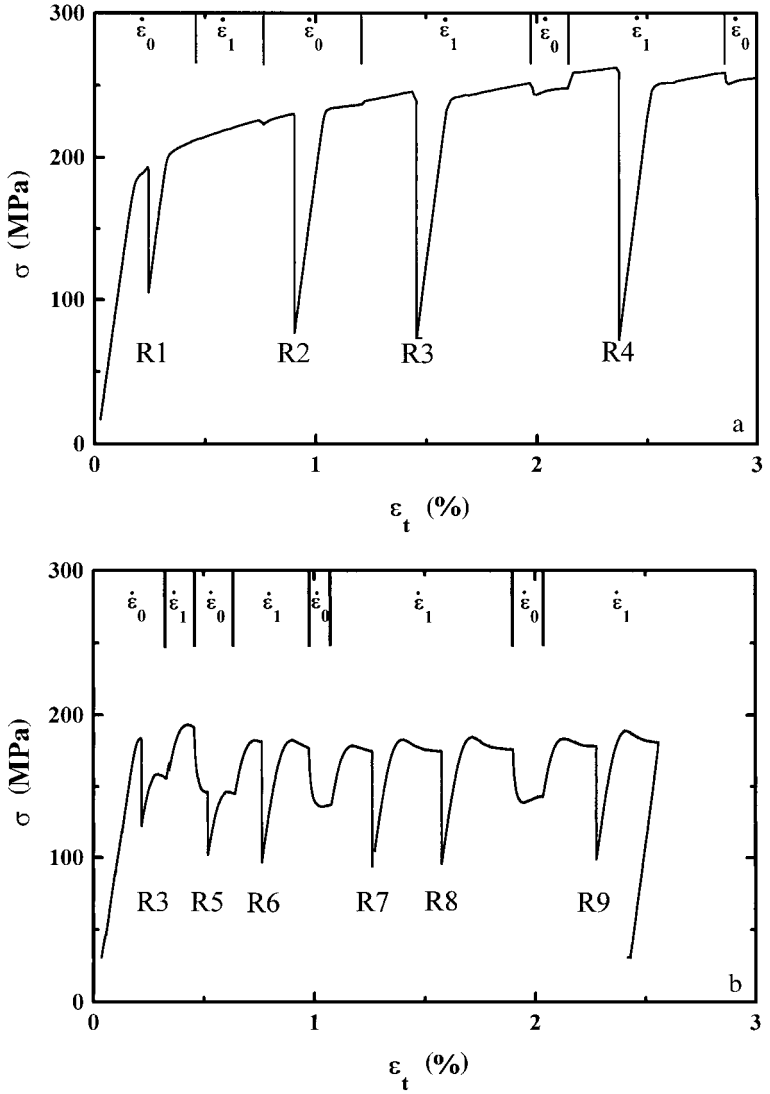

Fig. 3. Stress–strain curves of samples deformed along $[1\bar{1}2]$ at 1400 °C. a) High strain rates $\dot{\varepsilon}_0 = 10^{-4}$ 1/s and $\dot{\varepsilon}_1 = 5 \times 10^{-4}$ 1/s. b) Low strain rates $\dot{\varepsilon}_0 = 10^{-6}$ 1/s and $\dot{\varepsilon}_1 = 5 \times 10^{-6}$ 1/s. Stress relaxation tests are marked by R. The SRC experiments with changes between $\dot{\varepsilon}_0$ and $\dot{\varepsilon}_1$ are marked by vertical lines

1400 °C before it was reloaded. In Fig. 4a, the respective values of I are connected by a dotted line and show the strong dropping after the annealing and the re-increasing on further straining.

In order to support the results of the SRC tests by experiments of different kinetics, stress relaxation tests (R) were performed between the SRC tests. While at high strain rates the SRC experiments indicate a small strain rate sensitivity I, the corresponding relaxation tests result in very large drops of the flow stress, as demonstrated by Fig. 3a.

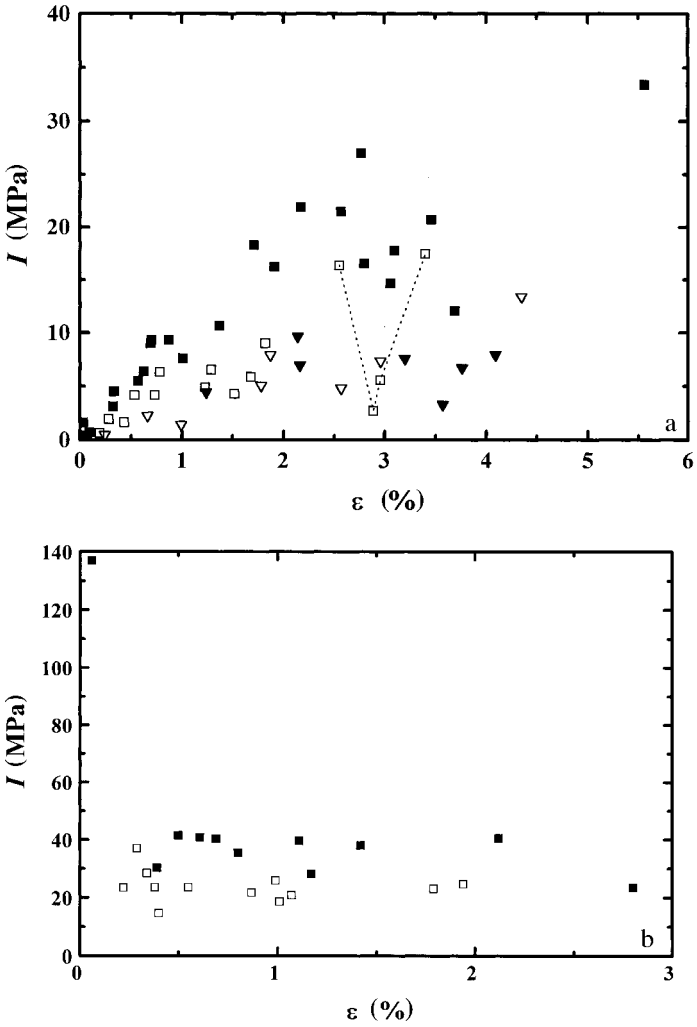

Fig. 4. Strain rate sensitivity I versus plastic strain ε determined by stress relaxation tests (full symbols) and by SRC experiments (open symbols) at 1400 °C along $[1\bar{1}2]$. a) High strain rates: □ 10^{-4} 1/s, ▽ 5×10^{-4} 1/s. b) Low strain rates: □ 10^{-6} 1/s

This is usually due to a high strain rate sensitivity. This apparent contradiction follows from the particular shape of the relaxation curves. Fig. 6a and b present three relaxation curves each of two specimens with increasing strain. Particularly at small strains, the curves comprise two distinctive parts, a steep part at the beginning of the tests at high stresses and correspondingly high strain rates, and a flat part at lower stresses or correspondingly low strain rates. As described in Section 2, the inverse slope of the relaxation curves equals the strain rate sensitivity *I,* which is low at high strain rates, and vice versa, fully agreeing with the results of the SRC tests. With increasing strain, the flat part moves up to higher strain rates, obviously concealing the steep part as demonstrated in Fig. 6a. Finally, the flat parts of different relaxation curves coincide as

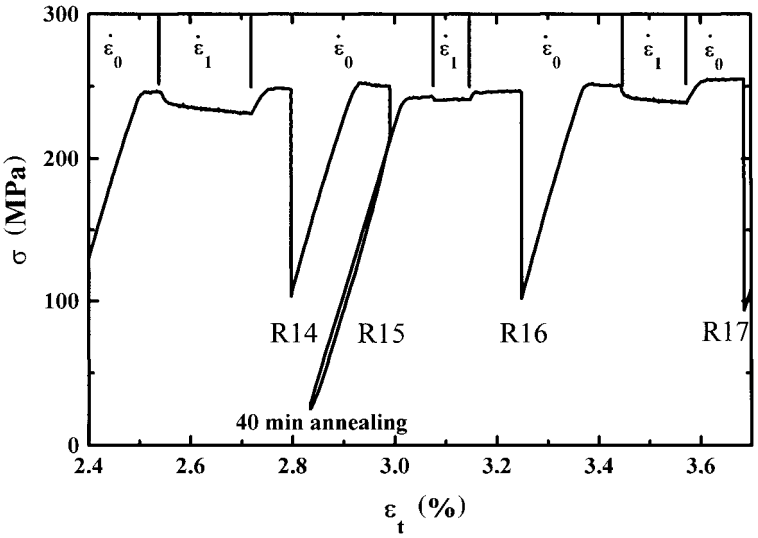

Fig. 5. Detail of a stress–strain curve of a sample deformed at 1400 °C along $[1\bar{1}2]$ with SRC experiments and stress relaxation tests (R). $\dot{\varepsilon}_0 = 1.2 \times 10^{-4}$ 1/s and $\dot{\varepsilon}_1 = 0.5 \times 10^{-4}$ 1/s. After the relaxation R15 the sample was unloaded, annealed under a small constant load for 40 min and then reloaded

in Fig. 6b, whereas the steep part moves to higher stresses due to work hardening, getting less prominent. The slopes of the three lines in Fig. 6b represent the results of SRC experiments performed just before the respective stress relaxation tests. These lines fit quite well to the relaxation curves, underlining the agreement between the results of SRC and stress relaxation tests. At a certain stress, the slope of the relaxation curves and the corresponding strain rate sensitivity I seem to be a unique function of the strain

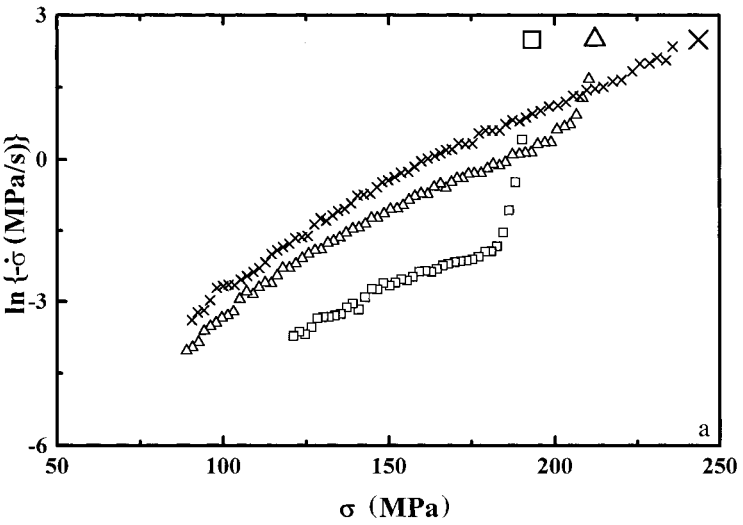

Fig. 6

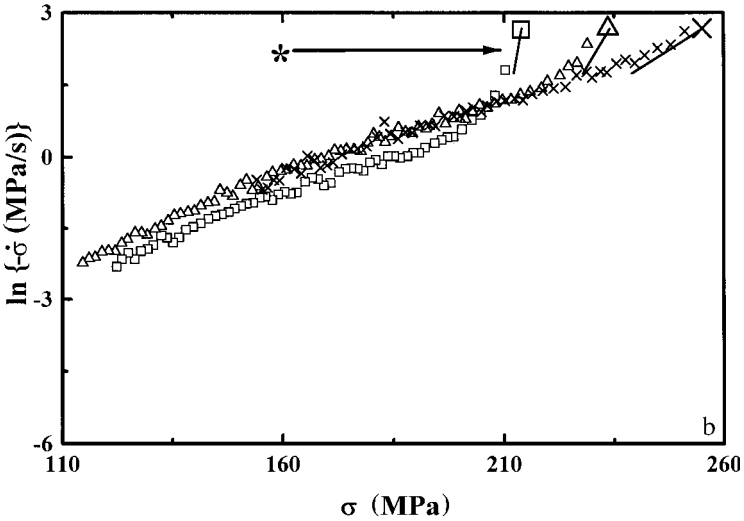

Fig. 6. Relaxation curves of samples deformed at 1400 °C along [1$\bar{1}$2] to different strains at high strain rates. Large symbols denote data calculated as described in Section 2. Lines correspond to SRC experiments just before the respective stress relaxation test. a) $\dot{\varepsilon}_0 = 10^{-4}$ 1/s; □ R1 at 0.03%, △ R2 at 0.32%, × R6 at 2.17%. b) Same sample as in Fig. 5 with $\dot{\varepsilon}_0 = 1.2 \times 10^{-4}$ 1/s; □ R9 at 0.33%, △ R14 at 1.37%, × R20 at 3.46%

rate as outlined in Fig. 7 for an intermediate plastic strain of 1.4 %, irrespective of the initial strain rate.

The values of the strain rate sensitivity I from stress relaxation tests are included in the summary of Fig. 4 as full symbols. Here, the data points are derived at the beginning of each relaxation test, i.e. they should correspond to the strain rate before the

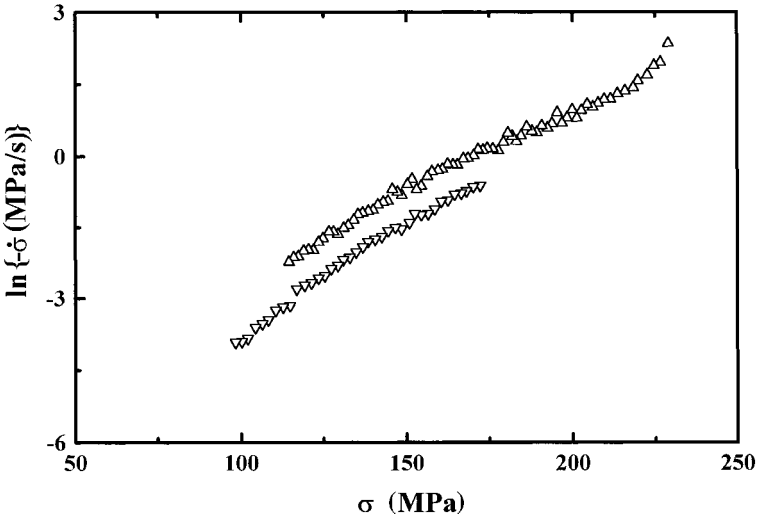

Fig. 7. Comparison of relaxation curves of experiments along [1$\bar{1}$2] at 1400 °C using different strain rates, both after a plastic strain of 1.4%. △ $\dot{\varepsilon}_0 = 1.2 \times 10^{-4}$ 1/s, ▽ $\varepsilon = 5 \times 10^{-6}$ 1/s

relaxation tests. Fig. 4a demonstrates the increase of the strain rate sensitivity I with increasing strain from almost zero up to about 30 MPa for a starting strain rate of 10^{-4} 1/s, as discussed above for the SRC experiments. This increase represents the growing dominance of the flat part of the relaxation curves with increasing strain. Fig. 4a shows also data for the higher strain rate of 5×10^{-4} 1/s. As expected, they are smaller than those for 10^{-4} 1/s. The results for small strain rates are summarized in Fig. 4b.

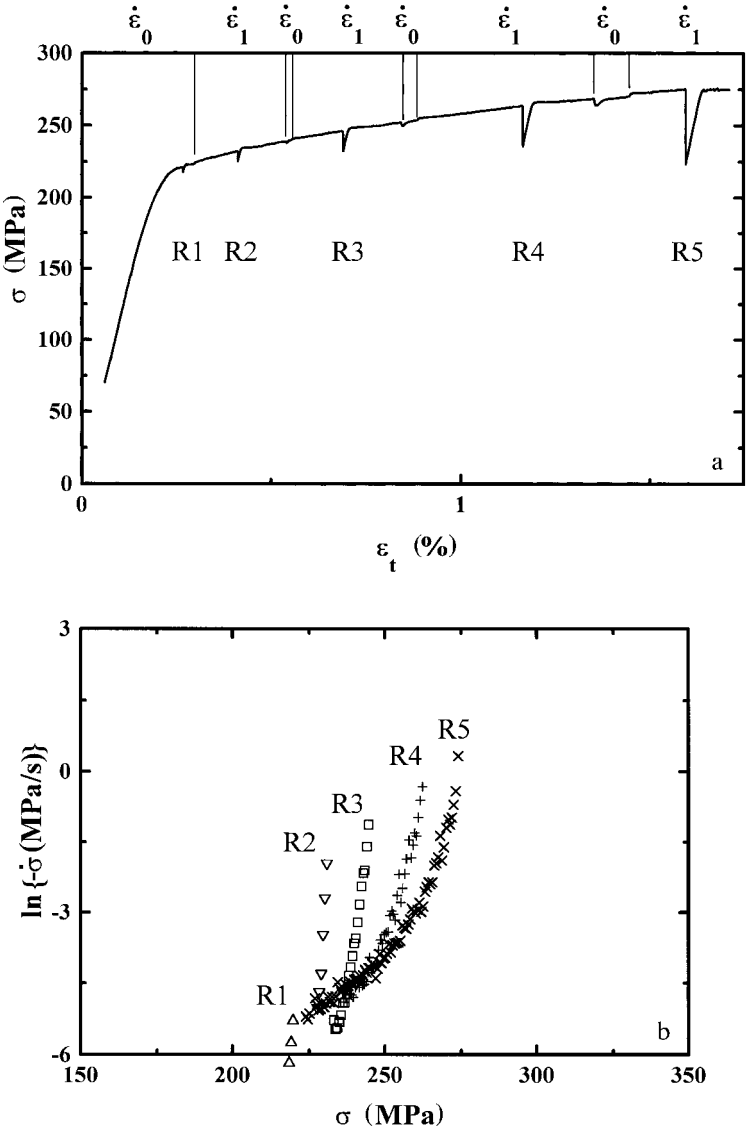

Fig. 8. Results of an experiment at 1200 °C with a $[1\bar{1}2]$ compression axis at $\dot{\varepsilon}_0 = 10^{-6}$ 1/s and $\dot{\varepsilon}_1 = 10^{-5}$ 1/s. a) Stress–strain curve. b) Relaxation curves at 0.08% (R1), 0.21% (R2), 0.48% (R3), 0.93 % (R4), 1.35 % (R5)

The strain rate sensitivity I amounts to about 30 MPa and seems to be independent of the strain. In general, I values of relaxation tests are larger than those of SRC tests at the same (geometrical) mean velocity. Fig. 4b contains also a single data point with a very high strain rate sensitivity of 140 MPa resulting from the relaxation R3 of Fig. 3b, performed just at the upper yield point. As it will be described below, a similar phenomenon was observed also during deformation along [100].

At 1200 °C, SRC and stress relaxation tests show low strain rate sensitivities I also at low strain rates, which slightly increase with strain as demonstrated in Fig. 8. At low strains, the relaxation curves are very steep as, e.g., R1 and R2 in Fig. 8b. The values of I increase from about 0.6 to 2.1 MPa. At higher strains, the relaxation curves exhibit a flat part at lower strain rates comparable to the behaviour at 1400 °C. However, this feature occurs at much higher strains.

3.2 Deformation along [100]

As described in the Introduction, some specimens were deformed along [100] in order to suppress slip on {100} planes, which are the primary planes for the deformation along $[1\bar{1}2]$ [2]. As shown in Fig. 9, at 1400 °C the stress–strain curves exhibit a yield point effect followed by a zero work-hardening region. While the curve for $\dot{\varepsilon} = 10^{-6}$ 1/s is most similar to that of specimens deformed along $[1\bar{1}2]$ at the same small strain rate, for $\dot{\varepsilon} = 1 \times 10^{-4}$ l/s the flow stress is about 50 % higher. At the fast strain rate, a pronounced yield point does not only occur during the first loading but also after stress relaxation experiments, which differs from the behaviour at loading in $[1\bar{1}2]$ direction.

The relaxation curves of experiments with a [100] orientation, shown in Fig. 10, do not exhibit the two-stage shape of those with a $[1\bar{1}2]$ orientation. Even at high strain rates, they have a simple convex shape. Analogous to the deformation in $[1\bar{1}2]$ direction,

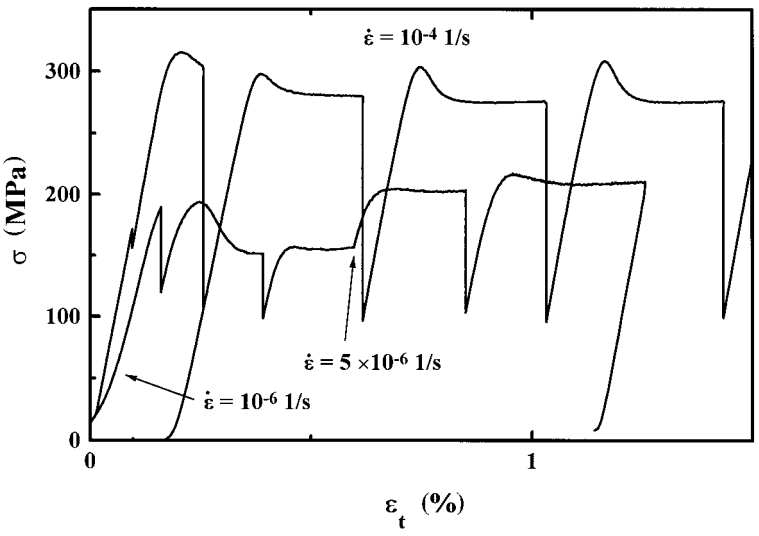

Fig. 9. Stress–strain curves of two samples deformed at 1400 °C along [100] at a high strain rate ($\dot{\varepsilon} = 10^{-4}$ 1/s) and at low ones ($\dot{\varepsilon} = 10^{-6}$ and 5×10^{-6} 1/s) including several stress relaxation tests and one SRC experiment

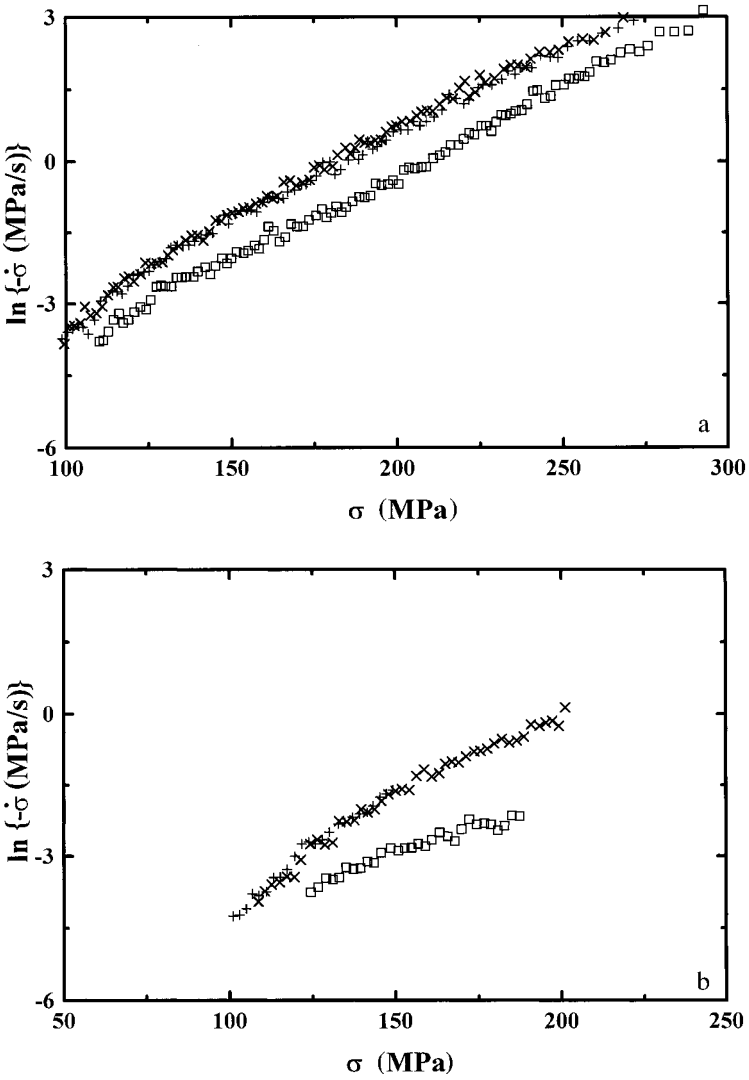

Fig. 10. Relaxation curves of experiments at 1400 °C along [100]. a) $\dot{\varepsilon} = 1 \times 10^{-4}$ 1/s; □ 0.12%, + 0.5%, × 0.92%. b) $\dot{\varepsilon} = 10^{-6}$ 1/s and 5×10^{-6} 1/s; □ 0.04 %, + 0.29 %, × 0.72 %

the relaxation curves are shifted upwards with increasing strain, reaching a final position. In Fig. 10b, the very flat relaxation curve at a strain of 0.04% is the result of a stress relaxation test just before the upper yield point. It again corresponds to $I = 140$ MPa, well agreeing with a similar result for the deformation along $[1\bar{1}2]$, discussed above. Fig. 11 summarizes all values of I, for fast and slow deformation along [100]. After some strain, a value of about 40 MPa is reached.

At lower temperatures, deformation along [100] results in an unstable stress–strain curve as shown in Fig. 12 for 1150 and 1120 °C. All four stress relaxation tests and the three SRC experiments are marked. All the other stress drops occurred during the defor-

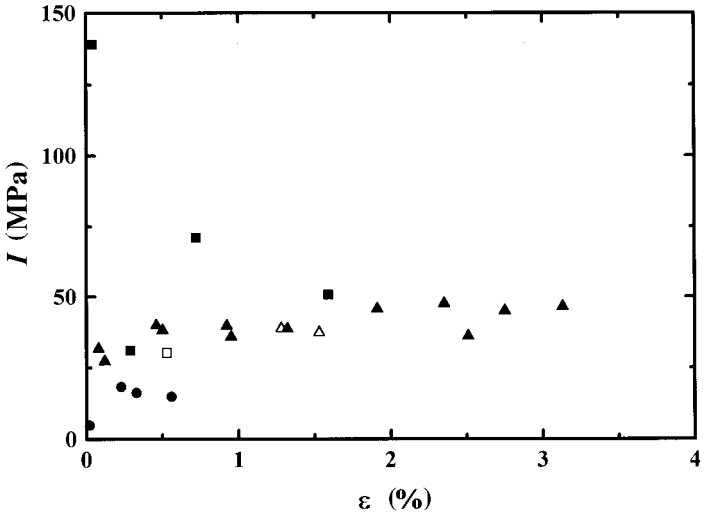

Fig. 11. Strain rate sensitivity I of samples deformed along [100]. Squares: 1400 °C, 10^{-6} 1/s; triangles: 1400 °C, 10^{-4} 1/s; circles: 1150 °C, 10^{-6} 1/s. Full symbols: relaxation tests, open symbols: SRC tests

mation at constant strain rate. In Fig. 13, the optical micrographs of the specimen show that these instabilities are not due to fracture but should be real serrations. The strain rate sensitivity I determined from stress relaxation tests at 1150 °C, included in Fig. 11, amounts to about 16 MPa and is therefore smaller than at 1400 °C but remarkably higher than for deformation along $[1\bar{1}2]$.

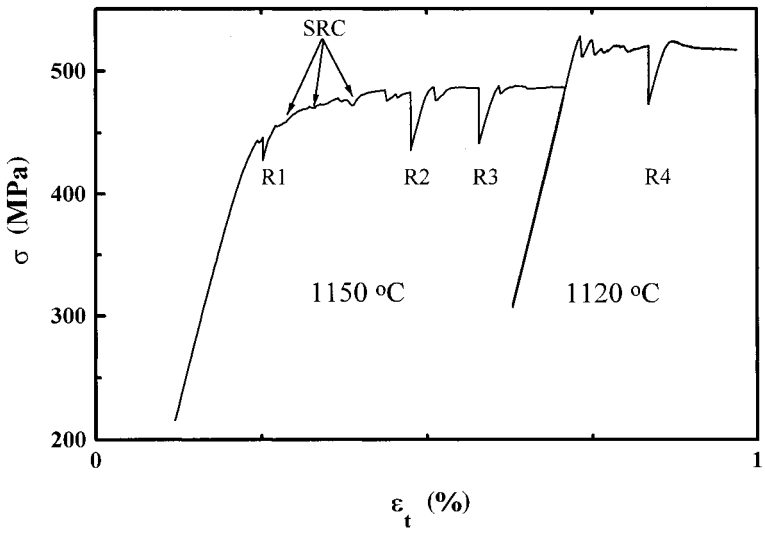

Fig. 12. Stress–strain curve of a sample deformed along [100] at 1150 and 1120 °C at a basic strain rate of 10^{-6} 1/s, including some stress relaxation tests (R) and SRC experiments (marked by arrows)

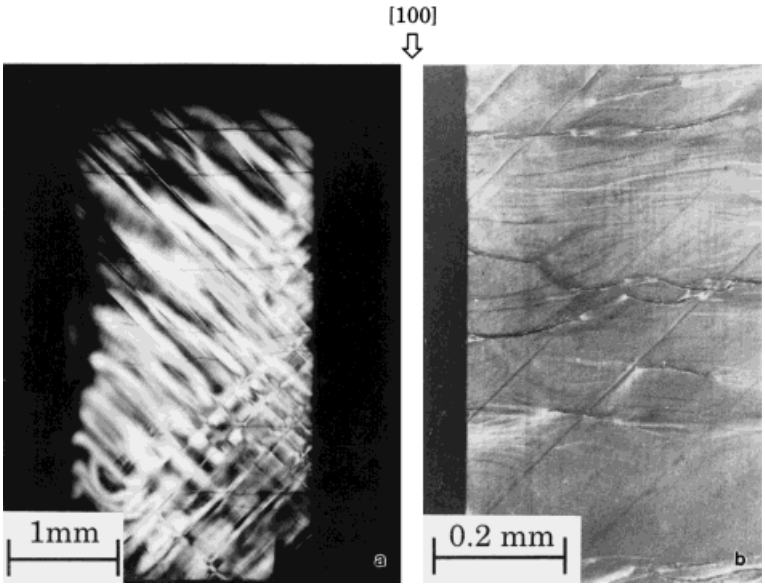

Fig. 13. Optical microscopy images of a (010) side face of a sample deformed along [100] at 1150 °C. a) Birefringence patterns, b) surface relief

Summarizing these results, distinct differences are observed between the deformation along [100] and $[1\bar{1}2]$. Between 1150 and 1400 °C, the flow stress depends more strongly on the temperature in [100] orientation than in $[1\bar{1}2]$ orientation. Accordingly, the strain rate sensitivity I is higher, too.

The activated slip planes can be deduced from deformed samples using optical microscopy. Fig. 13 shows the (010) side face of the sample deformed in [100] direction at 1150 °C. The birefringence patterns of Fig. 13a show contrasts oriented in [101] and $[10\bar{1}]$ directions. Changing the focus of the microscope does not shift these patterns suggesting $(10\bar{1})$ and (101) slip planes. The horizontal high-contrast wavy lines, also shown in the surface relief of Fig. 13b, can be explained by surface steps originating from screw dislocations on (110) or $(1\bar{1}0)$ planes. Viewing on the other side faces yields the same result. Thus, it may be concluded that all four possible {110} glide planes are activated. Fig. 13a proves that the deformation is not homogeneous. The wavy structure of the surface steps in Fig. 13a, and in more detail in Fig. 13b, is certainly due to the mutual cutting of slip bands or to cross slip. Fig. 13b displays also some straight lines in ⟨110⟩ direction of sharp contrast. These surface steps cannot be explained by glide on {110} planes, but suggest that slip on {111} planes had been activated as well.

4. Results of TEM Observations

4.1 TEM observation of samples deformed along $[1\bar{1}2]$

As described in Section 2, specimens were cooled from the deformation temperature either in the unloaded state or under load in order to study the influence of the cooling treatment on the dislocation structures observed at room temperature. Fig. 14 shows the respective dislocation structures of two samples deformed at 1400 °C at comparable

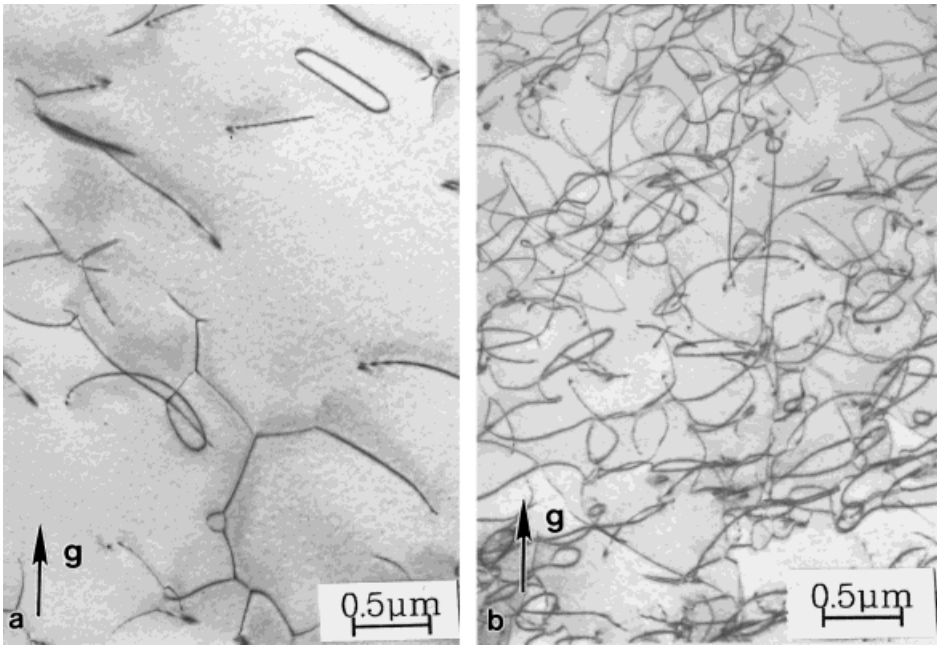

Fig. 14. Dislocation structure of samples deformed along $[1\bar{1}2]$ at 1400 °C up to a plastic strain of about 2.5%. In both micrographs the zone axis is near the $[\bar{1}11]$ foil normal, and the **g** vector is [202] or $[02\bar{2}]$ so that all relevant dislocations should be visible. a) Cooled in unloaded condition, b) cooled under full load

plastic strains of about 2.5%. Obviously, these two different procedures result in different dislocation densities and morphologies. As the dislocation density is much lower in Fig. 14a than in Fig. 14b, recovery during cooling without load should have reduced the dislocation density so that Fig. 14b represents the dislocation structure during the deformation better than Fig. 14a does. Therefore, all the other micrographs are taken of specimens cooled under load.

At strains above about 1%, cubic zirconia deforms by multiple slip. Fig. 15 shows the dislocation structure of a sample deformed at 1400 °C along $[1\bar{1}2]$ using different **g** vectors. The primary dislocations of $1/2[1\bar{1}0]$ Burgers vector are in contrast only in Fig. 15a. These dislocations appear smoothly curved on their inclined (001) slip plane. Stereo pairs prove that the dislocations are sometimes not arranged exactly on their slip planes indicating the action of cross slip or climb. The only pinning agents acting on the primary dislocations seem to be the other two sets of dislocations, which can clearly be discerned in Figs. 15b to d. The Burgers vectors of these secondary dislocations are $1/2[01\bar{1}]$ (extinguished in Fig. 15c) and 1/2[101] (extinguished in Fig. 15d). These secondary dislocations are mainly of screw character so that they are imaged as quite straight lines.

Stereo pairs of transmission electron micrographs were used to determine the glide plane of these dislocations. Due to their straightness and mainly screw character this was possible only in few cases, where the inclination and the Burgers vectors suggested (010) 1/2[101] and (100) $1/2[0\bar{1}1]$ systems. Besides, the activated slip planes were determined by wide-angle tilting experiments. Fig. 16 shows the same specimen area imaged

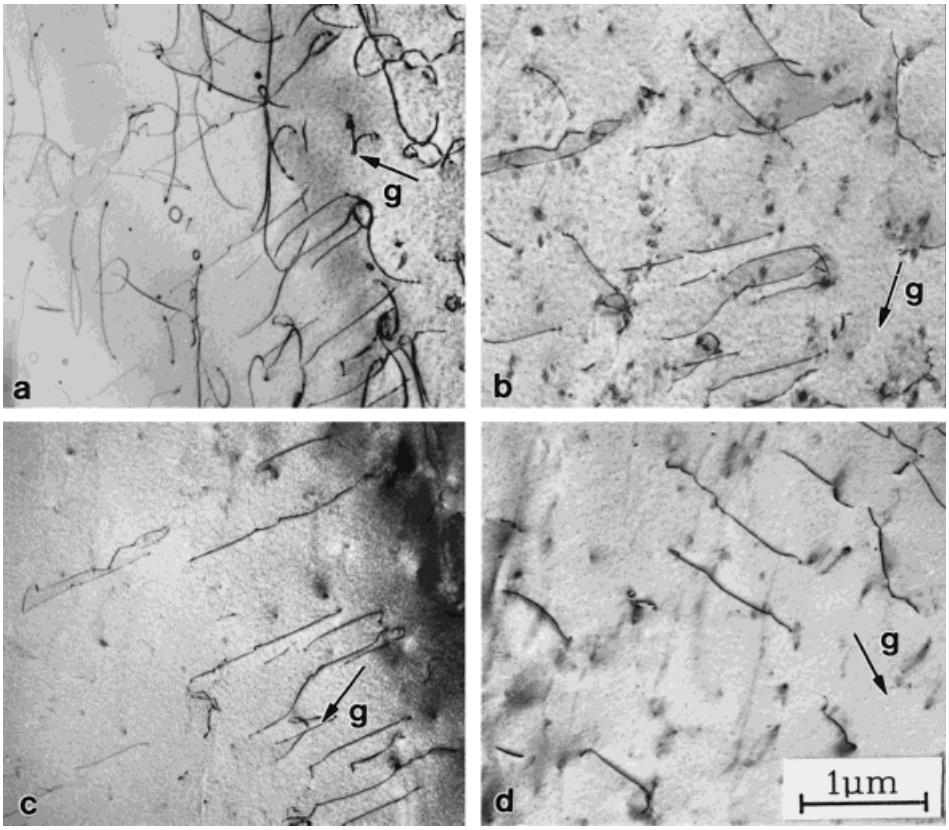

Fig. 15. Dislocation structure of a sample deformed along $[1\bar{1}2]$ at 1400 °C up to a plastic strain of 3% and cooled under full load. a) $\mathbf{g} = [0\bar{2}2]$ near the $[\bar{1}11]$ pole; primary and secondary dislocations visible. b) $\mathbf{g} = [220]$ near the $[\bar{1}11]$ pole; primary dislocations extinguished, secondary ones visible. c) $\mathbf{g} = [111]$ near the $[\bar{2}11]$ pole; primary and secondary dislocations with $\mathbf{b} = 1/2[01\bar{1}]$ extinguished, secondary ones with $\mathbf{b} = 1/2[101]$ visible. d) $\mathbf{g} = [11\bar{1}]$ near the $[\bar{1}21]$ pole; primary and secondary dislocations with $\mathbf{b} = 1/2[101]$ extinguished, secondary ones with $\mathbf{b} = 1/2[01\bar{1}]$ visible

near the $[00\bar{1}]$, $[1\bar{1}\bar{1}]$ and $[1\bar{1}0]$ poles. Using the [220] **g** vector, dislocations of the primary slip system are extinguished and only those of the secondary systems are visible. Near the $[00\bar{1}]$ pole in Fig. 16a, the (100) and (010) planes are oriented edge-on. Here, the dislocations appear as rather straight lines running parallel to the traces of these planes. However, in Fig. 16c taken near the $[1\bar{1}0]$ pole, these dislocations are curved. As the (111) and $(11\bar{1})$ planes are edge-on at this pole, the secondary dislocations cannot be arranged on these planes. Although the Schmid factor of 0.35 of the (010) $1/2[101]$ and (100) $1/2[0\bar{1}1]$ systems is smaller than that of 0.41 for glide on {111} planes, the glide on the cube planes seems to be favoured because of their smaller glide resistance.

The dislocation density of the primary system is 1.4×10^{13} m^{-2} and that of the other slip systems is about 5×10^{12} m^{-2}. As shown in Fig. 17a, the dislocations of different systems may interact resulting in the formation of junctions, which may act as obsta-

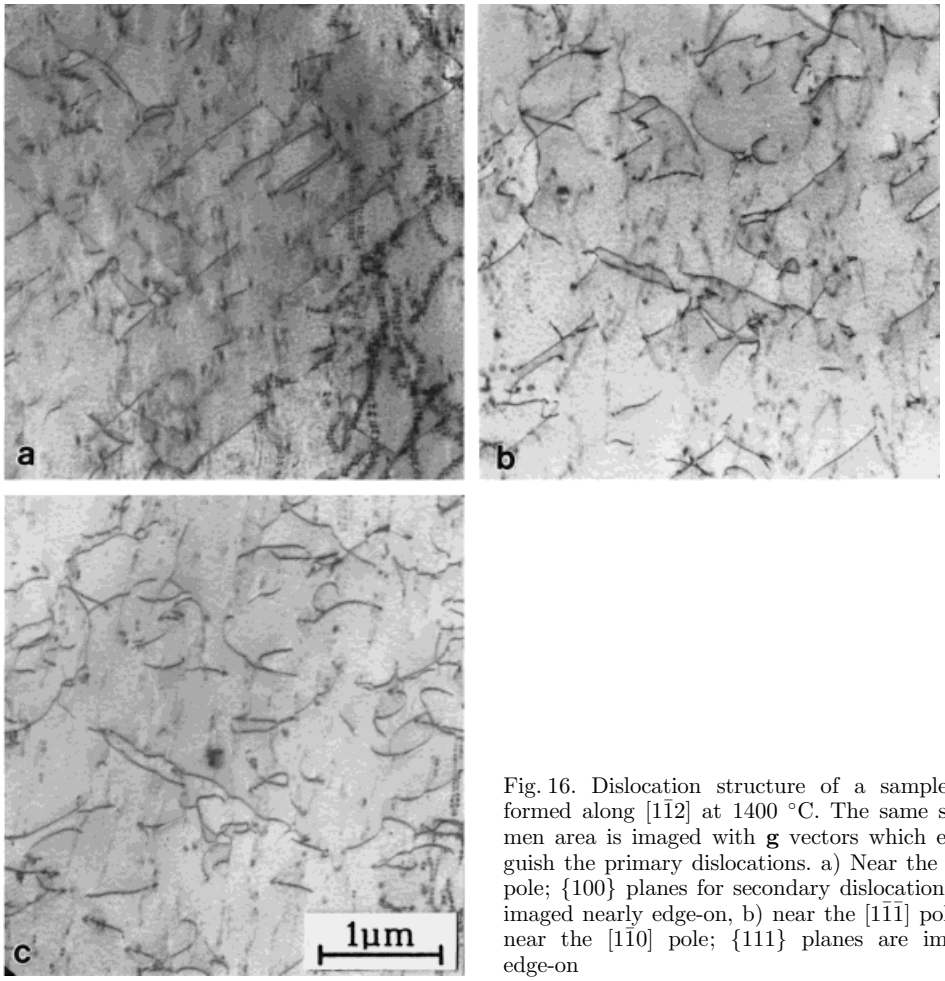

Fig. 16. Dislocation structure of a sample deformed along $[1\bar{1}2]$ at 1400 °C. The same specimen area is imaged with **g** vectors which extinguish the primary dislocations. a) Near the $[00\bar{1}]$ pole; {100} planes for secondary dislocations are imaged nearly edge-on, b) near the $[1\bar{1}\bar{1}]$ pole, c) near the $[1\bar{1}0]$ pole; {111} planes are imaged edge-on

cles. The secondary dislocations of Fig. 17b have high jogs, which should also impede the dislocation motion. The link lengths between both the junctions and the jogs are between 1 and 2.5 µm.

4.2 TEM observation of samples deformed along [100]

The result described in Section 3.2, obtained by optical microscopy, that mainly {110} planes are activated during deformation along [100] is corroborated also by TEM. Fig. 18 shows micrographs taken with different **g** vectors of a sample deformed at 1400 °C by about 2 %. Viewing approximately in [001] direction reveals two sets of relatively straight dislocations appear in $[1\bar{1}0]$ and [110] directions, which are extinguished for $\mathbf{g} = [220]$ (Fig. 18b) and $\mathbf{g} = [\bar{2}20]$ (Fig. 18c), respectively. Besides, more curved dislocations occur, which disappear at $\mathbf{g} = [020]$. Sets of stereo micrographs and further tilting experiments prove that most of the straight dislocations are arranged on (110) and $(1\bar{1}0)$ slip planes, which are imaged edge-on, having $1/2[\bar{1}10]$ and $1/2[110]$ Burgers vec-

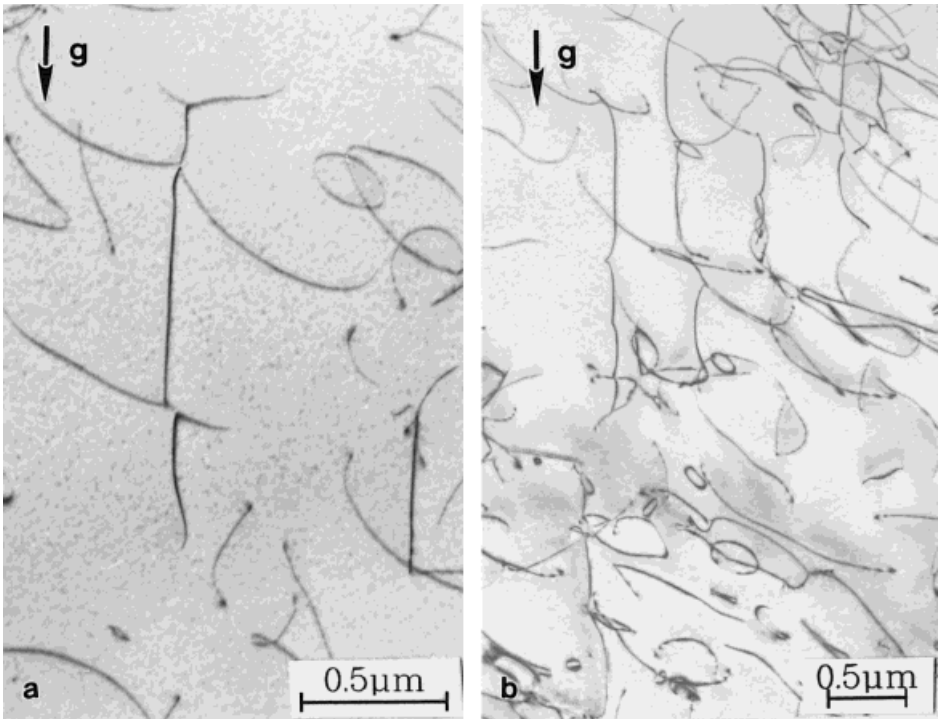

Fig. 17. Dislocation structure of the same sample as in Fig. 14b. a) Interaction between dislocations of different slip systems, b) jogged dislocations of a secondary system

tors. Most probably, the curved dislocation structures belong to the inclined (101) and $(\bar{1}01)$ planes with $1/2[10\bar{1}]$ and $1/2[101]$ Burgers vectors. Only a few dislocations have other Burgers vectors, which in Fig. 18a are extinguished by the [200] **g** vector. Consequently, most of the deformation along [100] is carried by dislocations on the four equivalent slip systems on {110} planes. They have the maximum orientation factor of 0.5. The dislocations strongly bow out, apparently owing to mutual interaction between dislocations of different glide systems.

5. Discussion

In the following Sections 5.1 to 5.4 some relevant processes are outlined. A model of the deformation of cubic zirconia at high temperatures is described in Section 5.5. Finally, the macroscopic deformation behaviour is discussed, i.e. for deformation along $[1\bar{1}2]$ in Section 5.6 and for deformation along [100] in Section 5.7.

5.1 Recovery and the relevance of observed dislocation structures

As it was shown in Section 4.1, it is essential to consider the history of the samples during cooling in order to correctly interpret the observed dislocation structures. It was assumed in [4] that rapid cooling to below 1000 °C in about 15 min is sufficient to avoid remarkable recovery. However, other experiments suggest that diffusive and dynamic recovery are important already at 1400 °C [5, 18, 19]. Fig. 14 of Section 4.1 clearly

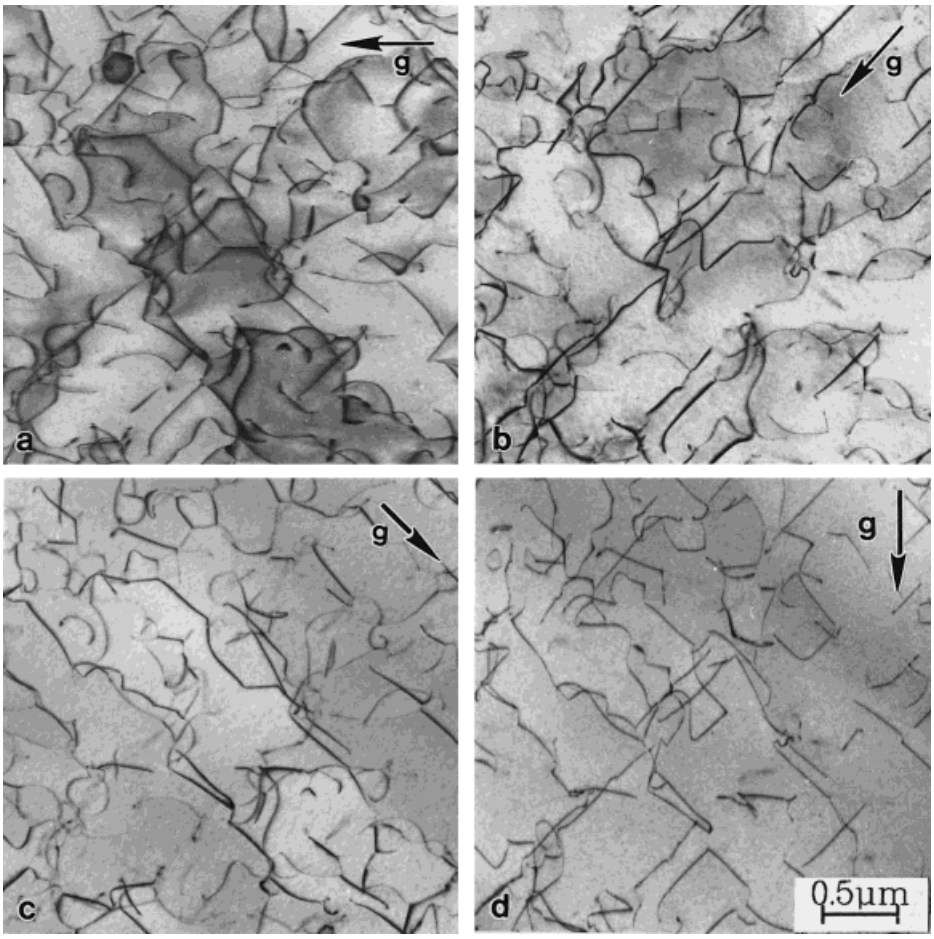

Fig. 18. Dislocation structure of a sample deformed at 1400 °C along [100]. Images taken near the [001] zone axis with a) $\mathbf{g} = [200]$; b) $\mathbf{g} = [220]$, $\mathbf{b} = 1/2[1\bar{1}0]$ extinguished; c) $\mathbf{g} = [\bar{2}20]$, $\mathbf{b} = 1/2[110]$ extinguished; d) $\mathbf{g} = [020]$, $\mathbf{b} = 1/2[101]$ and $1/2[10\bar{1}]$ extinguished

shows the difference between the dislocation densities and structures imaged after cooling the specimens in the unloaded state and under full load. This proves that recovery has to be considered in interpreting the TEM micrographs and as an essential process during the deformation of cubic zirconia, as it will be done in Section 5.5. As all micrographs of this paper, except Fig. 14a, are taken of specimens cooled under load, they should represent the real dislocation structures far better than those in previous papers. Recovery during cooling certainly is the reason that dislocation densities in the literature differ by about one order of magnitude, e.g. samples deformed by a few per cent showed dislocation densities between 3.0×10^{12} m^{-2} [4] and 2.5×10^{13} m^{-2} [1].

5.2 Operative slip systems

The results of Section 4.1 presented on the active slip systems partly contradict those in the literature. It is generally accepted that the deformation of cubic zirconia single crystals

in [1$\bar{1}$2] direction first activates the primary (001) 1/2[1$\bar{1}$0] slip system (e.g., [1, 3, 4]). At higher strains secondary slip systems were additionally observed having 1/2[0$\bar{1}$1] and 1/2[101] Burgers vectors [4, 5]. Contrary to previous investigations [3 to 5], in the present study the secondary dislocations with these Burgers vectors are arranged on (100) and (010) planes, but not on those of {111} type. Secondary {100} slip planes are in accordance with the results of *in situ* tensile tests in [1$\bar{1}$2] direction inside the HVEM at about 870 °C [15]. Berg-Barett topography gives some indication of the existence of (100) 1/2[0$\bar{1}$1] and (010) 1/2[101] slip systems [3]. However, especially the dislocation structures observed by TEM were usually discussed assuming {111} slip planes. In many cases the interpretation of the dislocation structures is not unambiguous, though. For example, the character of the slip bands of secondary dislocations of Fig. 4 in [5] should be crititically checked again. In [6], the critical resolved shear stress for slip on {111} and {110} planes was found to be about 1/3 higher than that for {001} planes. It is therefore not surprizing that, because of their lower glide resistance, (100) and (010) planes are activated as secondary slip planes, inspite of their smaller orientation factor (viz. 0.35, instead of 0.41).

For the deformation along [100], the operating slip systems have not yet been investigated in detail. To the authors' knowledge, only first results of TEM investigations are published of samples deformed at 400 °C [13] and 1300 °C [2], where {111} 1/2⟨110⟩ slip systems were claimed to operate. As Fig. 13 shows, some light microscope slip traces point at the action of these slip systems. However, Fig. 18 proves the dominance of the four equivalent slip systems on {110} planes. This is convincing as their orientation factor of 0.5 is higher than 0.41 of the systems with {111} planes, and as both systems are supposed to have similar critical resolved shear stresses [6]. This result is in accordance with *in situ* straining experiments at 1150 °C along [100], where two orthogonal {110} slip planes were activated [15].

Cube and non-cube slip planes greatly differ in the dynamic behaviour of dislocations, which is also shown by the *in situ* straining experiments at 1150 °C [15]. During deformation along [1$\bar{1}$2], the dislocations move on cube planes very jerkily over distances in the order of magnitude of the spacings between the dislocations, which corresponds to a very low strain rate sensitivity in corresponding macroscopic compression experiments [8, 9], and which may be called an athermal behaviour. On deformation along [100], the dislocations move on {110} planes in a viscous way. Hence, the present experiments are interpreted on the basis of the observation that the deformation along [1$\bar{1}$2] is mainly carried by dislocations on cube planes, whereas that along [100] is carried by dislocations on {110} planes, and that the different dynamic behaviour of dislocations on these planes is preserved up to 1400 °C.

5.3 Dislocation processes

In all materials, long-range dislocation interactions contribute to the flow stress. For the interaction between parallel dislocations, the so-called Taylor hardening [20], a formula of the contribution τ_i to the shear stress, considering the slip geometry of cubic zirconia, is given in [9, 10],

$$\tau_i = \alpha K b F_m \varrho^{1/2}/(2\pi) \,, \tag{4}$$

with α being a numerical factor of about 8, K, the energy factor of the respective dislocations (for slip on {100} planes at 1200 °C [10] equal to 67.7 GPa for screw and to

85.5 GPa for edge dislocations), b, the absolute value of the Burgers vector, and F_m, a normalized interaction constant depending on the dislocation character (for slip on {100} planes equal to 0.3 for screw and to 0.2 for edge dislocations). With the dislocation density of $\varrho = 1.4 \times 10^{13}$ m^{-2} of the primary slip system in Section 4.1, the long-range (athermal) part of the flow stress amounts to about $\tau_i = 33$ MPa for screw dislocations or to 28 MPa for edges. 30 MPa may be used as an average. This has to be compared with a resolved shear stress of about 90 MPa, if the flow stresses of about 200 MPa in the figures of Section 3.1 and the orientation factor of 0.47 of the primary slip system for the deformation along $[1\bar{1}2]$ are considered. The athermal shear stress inside the secondary systems with a dislocation density of 5×10^{12} m^{-2} amounts to only about $\tau_i = 20$ MPa, which is not additive to the athermal stress contribution of the primary system. The values for 1400 °C should be slightly lower but may be considered lower limits as the dislocation densities during deformation may be higher but are reduced by recovery, even in the specimens cooled under load.

As shown in Fig. 17a, dislocations of different slip systems may react to create junctions according to the Burgers vector reaction

$$1/2[1\bar{1}0] + 1/2[01\bar{1}] = 1/2[10\bar{1}]\,, \tag{5}$$

forming a three-dimensional dislocation network. The branches of the network can glide only if the stress is high enough to bow them out over the critical (half-loop) configuration. Using the terminology of eq. (4), this back stress is given by

$$\tau_b = Kb/(2\pi L)\,\ln\,(L/\beta r_0)\,, \tag{6}$$

where L is the link length, β is a numerical factor of about 5, and $r_0 \cong b$ is the inner cut-off radius of the dislocations. Using the experimental value of L of 1 to 2.5 μm in Section 4.1, the average of τ_b for screw and edge dislocations should be between about 13 and 28 MPa. The same estimation applies to the motion of jogs in screw dislocations. Thus, both mechanisms together may contribute at maximum about 40 MPa to the (shear) flow stress.

5.4 Chemical hardening

The deformation behaviour of earlier experiments at 1400 °C has been interpreted on the basis of solid solution hardening, which is the easiest way to explain the increase of the flow stress with increasing concentration of yttria [1, 7]. Y^{3+} ions may form associates with oxygen vacancies introduced to conserve the electrical neutrality. They were observed at low temperatures, should have a ⟨111⟩ symmetry axis [21, 22], and cause the Snoek effect observed by mechanical spectroscopy at temperatures between 200 and 500 °C [23, 24]. However, experiments up to 1200 °C have not indicated further associates in cubic zirconia [25]. It is supposed that these associates start to dissociate already above about 400 °C [26, 27] so that they cannot control the flow stress of cubic zirconia at 1400 °C.

Recently, an unusually high concentration of solved nitrogen as well as large ZrN precipitates were detected in samples deformed in argon atmosphere between 1600 and 1800 °C [28]. During deformation, solved nitrogen may interact with the dislocations forming Cottrell atmospheres [29]. Smaller ZrN precipitates might represent localized obstacles to the dislocation motion. However, such precipitates have never been ob-

served in specimens deformed between about 1000 and 1400 °C. As described above, *in situ* tensile tests inside an HVEM at 1150 °C [9, 10, 15] demonstrate that the dislocations of the primary slip system move very fast (flight velocity >50 μm/s) and that there is no indication of localized obstacles. This result should be true also for higher temperatures.

Thus, simple solid solution hardening models can obviously not be used to explain the dependence of the flow stress on the yttria concentration. It was stated in Section 5.1 and will be discussed in the following section that recovery is an essential process during the deformation of zirconia at high temperatures. Recovery by climb requires diffusion in both sublattices and is controlled by the species diffusing more slowly, which is the Zr^{4+} ion. Observations of dislocation loop shrinkage during annealing showed that the diffusion of Zr in an alloy with 18 mol% yttria is approximately 15 times slower than in an alloy with 9.4 mol%, with the activation energy being independent of the yttria concentration [30]. The reduced pre-exponential factor is explained by the trapping of the diffusing charged vacancy clusters at centres containing yttrium or the vacancies necessary for charge compensation. As first suggested in [7], a reduced diffusion may slow down the recovery kinetics leading to an increase of the flow stress with increasing yttria concentration.

5.5 Model of the deformation of cubic zirconia at high temperatures

Experimental observations which should be considered in a model are pointed out again:

– The observed microstructures do not indicate a particular mechanism of interaction between dislocations and other defects that may control the flow stress. Above about 1000 °C, the interaction with localized obstacles, which is important below about 800 °C [8], does not act any more.

– Long-range interaction between parallel dislocations (eq. (4)) yields an athermal flow stress part of at least $\tau_i \cong 30$ MPa (Section 5.3).

– Dislocation junctions and jogs in screw dislocations may contribute a back stress (eq. (6)) of $\tau_b \cong 40$ MPa at the most to the flow stress (Section 5.3). This contribution is also of athermal character.

– Recovery is an essential feature of high-temperature deformation of cubic zirconia already at 1400 °C (Section 5.1). It was suggested that diffusion-controlled processes govern the deformation above about 1450 to 1500 °C, for creep tests up to 1550 °C [16], and for tests at a constant strain rate up to 1750 °C [19]. The deformation is then governed by climb as in other ceramic materials (e.g. [31, 32]). Other authors (e.g. [17]) explain the high-temperature plasticity of cubic zirconia by a link length model including recovery. The particular model [33], however, is based on a viscous dislocation motion with a stress exponent of unity, which strongly contradicts the stress relaxation behaviour discussed in Section 5.6. Recovery may lead to reduced dislocation densities in TEM samples compared to the state during deformation, even of specimens cooled under load. As a consequence, the dislocation densities measured after creep experiments follow a dependence on stress as eq. (4), but with a numerical constant $\alpha F_m/(2\pi)$ twice the value above characteristic of work-hardening [34]. Thus, for deformation along $[1\bar{1}2]$, $\tau_i + \tau_b$ may be larger than estimated and represent the macroscopic flow stress. Such a situation was already observed for the athermal deformation range around 1150 °C [9, 15].

– The dynamic behaviour of dislocations moving on the cube and on the non-cube (most probably {110}) planes greatly differs (Sections 4 and 5.2). The dislocations experience very little resistance on cube planes, which corresponds to a low strain rate sensitivity. In contrast to that, measurements of the dislocation velocities on cube planes by the stress pulse-etching technique between 1150 and 1450 °C revealed a high strain rate sensitivity [35]. However, these experiments were performed at low stresses, corresponding to dislocation velocities which are about ten orders of magnitude lower than those in macroscopic deformation tests. Hence, these results are not relevant for the present study. On non-cube planes, the dislocations move in a viscous way. The viscous motion is certainly due to a lattice friction mechanism which is accompanied with a high strain rate sensitivity. The lattice friction mechanism may be the Peierls mechanism which is certainly influenced by the high concentration of the stabilizing yttria. The different dynamic behaviour is observed at 1150 °C [15], but should be preserved also up to higher temperatures.

As pointed out in [7, 9], the high-temperature plasticity of cubic zirconia can be understood on the basis of a phenomenological model described in [36, 37]. The dynamic law, i.e. the dependence of the strain rate $\dot{\varepsilon}$ on the applied stress τ, can be represented by the power law

$$\dot{\varepsilon} = \dot{\varepsilon}_0 (\tau/\tau_0)^m \,. \tag{7}$$

Here, τ_0 is a threshold stress, which is related to the long-range stress component $\tau_\mathrm{i} + \tau_\mathrm{b}$ in the order of magnitude of 100 MPa, $\dot{\varepsilon}_0$ is a constant, and m is the dynamic stress exponent; m need not be identical with the experimental stress exponent m^* defined in eq. (2). During straining, the microstructure changes. This is described by an evolution law

$$\mathrm{d}\tau_0/\mathrm{d}\varepsilon = \Theta_0 (1 - R\tau_0 \dot{\varepsilon}^{-1/n}) \,, \tag{8}$$

where Θ_0 is the initial work-hardening coefficient, and n is the strain-softening exponent. The latter term in the parentheses considers dynamic recovery via glide and climb, where R includes the diffusion coefficient. As described in Section 5.4, the diffusion coefficient strongly depends on the yttria concentration, which explains the dependence of the flow stress on the yttria concentration. Under steady state conditions as in creep, τ_0 is constant so that

$$\dot{\varepsilon}_\mathrm{ss} = (R\tau_0)^n = R' \tau^{n'} \,, \tag{9}$$

with $1/n' = 1/n + 1/m$. This is the well known creep law. In the present experiments at a constant strain rate, the work-hardening is low after the yield point so that eq. (9) should also account for the steady state flow stress. Equations (7) and (8) also describe transient phenomena as occurring in the stress relaxation experiments. For these experiments, eqs. (7) and (8) can be solved under the (well fulfilled) assumption that the actual stress τ is nearly equal to the threshold stress τ_0, yielding

$$m^* = \mathrm{d}\ln\dot{\varepsilon}/\mathrm{d}\ln\tau = \mathrm{d}\ln(-\dot{\tau})/\mathrm{d}\ln\tau = m - \frac{(m-n)\,A(\tau-\tau_1)}{(1-A)\,(\tau/\tau_1)^{m/n} + A(\tau/\tau_1)} \,, \tag{10}$$

with τ_1 being the stress at the beginning of the relaxation and

$$A = mC\Theta_0 R\tau_1 / [(m-n)\,(1 + C\Theta_0)\,\dot{\varepsilon}_1^{1/n}] \,.$$

C is the elastic compliance defined in Section 2. At the beginning of relaxation,

$$m^* = (\mathrm{d} \ln \dot{\varepsilon} / \mathrm{d} \ln \tau)_{\tau = \tau_1} = m(1 - A) + nA \,, \tag{11}$$

which is close to m for large m (and small A). At the end of the relaxation,

$$m^* = (\mathrm{d} \ln \dot{\varepsilon} / \mathrm{d} \ln \tau)_{\tau \ll \tau_1} = n \,. \tag{12}$$

Thus, the two-stage relaxation curves allow one to separate the dynamic dislocation properties from the recovery behaviour. In the following, some features of the deformation behaviour described in Section 3 are qualitatively discussed on the basis of the model. A quantitative description still has to be worked out.

5.6 Deformation along [1$\bar{1}$2]

According to Section 4.1, plastic deformation along [1$\bar{1}$2] should be explained solely by slip on primary and secondary {100} planes. As pointed out in Section 5.2, the glide resistance is low on these planes and the dislocations may move in an athermal way, corresponding to a large stress exponent m in eq. (7). This should be reflected in the strain rate sensitivity I.

The model of eqs. (7) to (12) predicts that the stress relaxation curves may show two distinct regions [37], particularly if ln $(-\dot{\sigma})$ is plotted versus ln σ. This was applied earlier to the stress relaxation kinetics in cubic zirconia [7, 9]. In the present experiments, stress relaxation curves were recorded with highly improved precision thus revealing the effect more clearly. Fig. 19 shows a respective plot of the data of Fig. 6 for low strains and high strain rates. In this plot, the slope of the curves corresponds to the apparent stress exponent m^* defined in eq. (2). Particularly, the first relaxation curve clearly shows the two stages. At high strain rates, the slope of the curves approximates the dynamic stress exponent m as shown in eq. (11), which is above 100 and describes the athermal behaviour of the gliding dislocations, observed earlier at lower temperatures [8

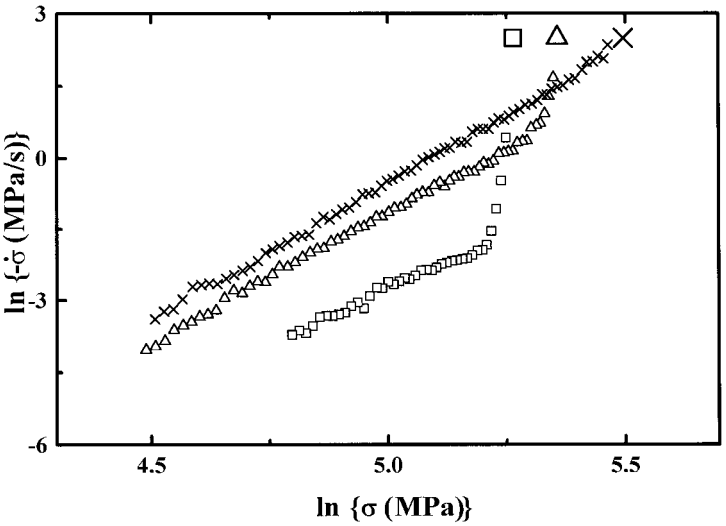

Fig. 19. Stress relaxation curves of Fig. 6a in a plot of ln $(-\dot{\sigma})$ versus ln σ

to 10]. The long tail at low strain rates describes the recovery appearing during relaxation. According to eq. (12), the slope of about four corresponds to the strain softening exponent n. This means that the relaxation curves are not recorded under the condition of a constant structure. In another sense, this holds true for the relaxation curves taken at the upper yield point. As indicated by the data points of Figs. 4b and 11, these relaxations yielded a very high strain rate sensitivity of about 140 MPa, which does not reflect the dynamic stress exponent m but a still strongly increasing density of mobile dislocations even during the relaxation tests.

With increasing strain, τ_0 rises owing to the increasing dislocation density. This makes the starting stress of the relaxation curves to rise as well as the recovery part to shift to higher strain rates. The dynamic part of the relaxation curves disappears at low starting strain rates as the lower curve of Fig. 7 shows.

At 1200 °C and small strains, the relaxation curves (R1 to R3) of Fig. 8b show only the steep part indicating a very low strain rate sensitivity. At larger strains with an increased dislocation density recovery also sets in. These curves demonstrate the transition between the athermal behaviour at about 1000 °C [8 to 10] to that at 1400 °C.

The dependence of the strain rate sensitivity I on the strain rate at 1400 °C, particularly at small strains, is also evident from the SRC experiments, compare Figs. 4a and b. It is therefore an intrinsic feature of the material. A value of I of about 30 MPa, which is typical of low strain rates and of larger strains at high strain rates, corresponds to a stress exponent of $m^* \cong 5$. This value agrees with earlier reports [2, 16, 18, 19]. Most of these results are derived from creep experiments with incremental load changes [16, 18, 19], all performed at small strain rates so that the dynamic stress exponent m could not be observed.

A characteristic feature of the stress–strain curves is the pronounced yield drop effect at small strain rates followed by zero work hardening as shown in Fig. 2. This behaviour is commonly believed to be characteristic of this material deformed along $[1\bar{1}2]$ at 1400 °C [1 to 3, 5]. However, as Fig. 2 also shows, the yield drop does not occur at higher strain rates but a weak work hardening is observed. This strain rate dependence of the shape of the stress–strain curves has not been discussed before, probably since most experiments were performed at a small strain rate of about 1.3×10^{-5} 1/s [1 to 3, 5]. Higher strain rates of 1.2×10^{-4} 1/s were used in [7], where the yield point effect is also missing. This, however, was not discussed by the authors. Usually, the yield point effect is explained by rapid dislocation multiplication during loading, which, however, in [4] was excluded, since the dislocation density did not strongly increase with strain. As discussed in Section 5.1, dislocation densities measured in specimens cooled in the unloaded state do not represent those during deformation. In [4] the yield drop effect is suggested to be due to the activation of secondary slip on {111} planes. This argument is, however, not convincing as the secondary slip planes are most probably also of {100} type (Sections 4.1 and 5.2). This should lead to an additional hardening. Dislocations on other secondary planes are even less mobile. In the present experiments, the occurrence of the yield drop effect during the deformation along $[1\bar{1}2]$ strongly depends on the strain rate. It does not appear at high strain rates, where the relaxation curves exhibit the steep part of athermal dislocation behaviour, but at low strain rates, where recovery is more important. At low strain rates and increasing τ_0, the recovery term in eq. (8) may exceed the hardening term so that $\mathrm{d}\tau_0/\mathrm{d}\varepsilon$ becomes negative, which explains the yield drop effect.

The result of the annealing experiment shown in Fig. 5 can be explained by the arguments discussed above. The specimen was unloaded after a plastic strain of about 2.8%, where τ_0 had already developed and recovery dominated the strain rate sensitivity. During annealing at 1400 °C for 40 min, the dislocation density and structure further recovered, reaching a state similar to that at the beginning of the deformation test. On reloading, the strain rate sensitivity is low again (see dotted line in Fig. 4a) but the flow stress is only slightly smaller than before annealing, owing to the athermal nature of the deformation at this high strain rate. Further straining re-establishes the deformed state.

5.7 Deformation along [100]

In this orientation, all slip systems with {001} glide planes are suppressed. Most probably, the dislocations glide on {110} planes, perhaps also on {111} ones. As described in Sections 5.2 and 5.5, the dislocations move in a viscous way on non-cube planes, which corresponds to larger values of the strain rate sensitivity I and lower values of the dynamic stress exponent m.

As a consequence, also at a high strain rate the stress relaxation curves of Fig. 10a do not show the two-stage behaviour characteristic of the deformation along $[1\bar{1}2]$ under the same conditions. In the plot of Fig. 20 of ln $(-\dot{\sigma})$ versus ln σ, the curves are slightly bent. The initial slope of $m^* \cong 9$ should again be close to the dynamic stress exponent characteristic of non-cube glide. The slope at the low stress end of $m^* \cong 6$ may again be equal to the strain softening exponent. In this case where the dynamic stress exponent m does not very much differ from the strain softening exponent n, both processes cannot clearly be separated. The high strain rate sensitivity is accompanied with a strong dependence of the flow stress on temperature, which is revealed by comparing the lower deformation curve at 1400 °C of Fig. 9 with that at 1150 °C of Fig. 12.

As shown in Fig. 9, at 1400 °C the stress–strain curves exhibit a yield point effect followed by a zero work-hardening region, not only for low strain rates (1×10^{-6} and

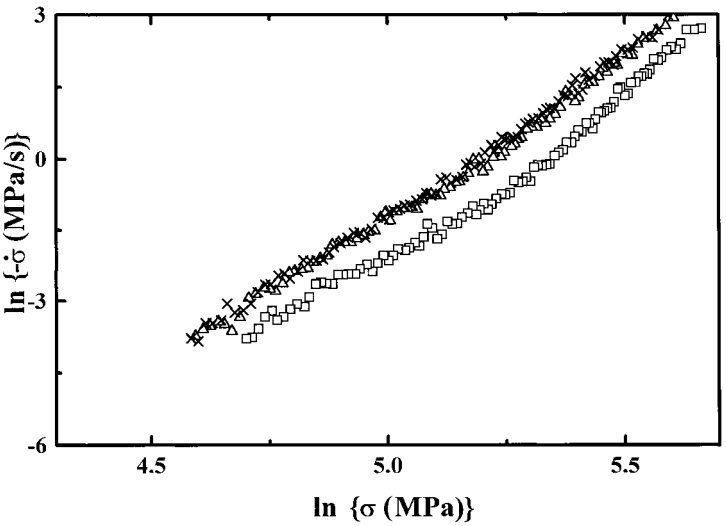

Fig. 20. Stress relaxation curves of Fig. 10a in a plot of ln $(-\dot{\sigma})$ versus ln σ

5×10^{-6} 1/s) but also for high ones (1×10^{-4} 1/s). This observation contradicts earlier reports (e.g., [2]), where initial slip on {100} planes was thought to be a prerequisite for the yield drop effect. In general, the yield drop should be more pronounced if the dynamic stress exponent is lower. This is in accordance with the appearance of a yield point effect for deformation along [100] with $m \cong 9$ also at a high strain rate and with its missing for deformation along $[1\bar{1}2]$ with $m > 100$ under the same conditions.

6. Conclusions

– At 1400 °C, stress–strain curves show a yield point effect followed by zero work hardening, which was thought to be typical of the deformation along $[1\bar{1}2]$, only at low strain rates. At high strain rates, continuous work-hardening occurs.

– The yield drop effect does not only appear during deformation along $[1\bar{1}2]$ but, contrary to earlier reports, also for deformation along [100] at low and high strain rates.

– For the deformation along $[1\bar{1}2]$, both the primary and the secondary slip planes are of {100} type. On these planes, the glide resistance is low, the dislocations move in an athermal way yielding a very high dynamic stress exponent.

– For the deformation along [100], the dominating slip planes are of {110} type. On these planes, the glide resistance is higher, the dislocations move with the aid of thermal activation which leads to a dynamic stress exponent of about nine.

– The deformation behaviour, particularly that during stress relaxation tests, is explained by the different dynamic properties of the dislocations and by the fact that recovery is an essential feature of the high-temperature deformation of cubic zirconia.

– According to the model, the two stages of the stress relaxation curves at low strains and high strain rates correspond to the dynamic behaviour of dislocations at the beginning, and to recovery at the end of the relaxation tests.

Acknowledgements The authors are grateful to Prof. Manfred Rühle for initiating the project. They thank him and Prof. Arthur H. Heuer for many stimulating discussions. Financial support by the Deutsche Forschungsgemeinschaft is gratefully acknowledged.

References

[1] A. Dominguez-Rodriguez, K. P. D. Lagerlöf, and A. H. Heuer, J. Amer. Ceram. Soc. **69**, 281 (1986).
[2] A. Dominguez-Rodriguez and A. H. Heuer, Cryst. Latt. Def. Amorph. Mater. **16**, 117 (1987).
[3] E. Fries, F. Guiberteau, A. Dominguez-Rodriguez, D.-S. Cheong, and A. H. Heuer, Phil. Mag. **A60**, 107 (1989).
[4] D.-S. Cheong, A. Dominguez-Rodriguez, and A. H. Heuer, Phil. Mag. **A60**, 123 (1989).
[5] D.-S. Cheong, A. Dominguez-Rodriguez, and A. H. Heuer, Phil. Mag. **A63**, 377 (1991).
[6] A. Dominguez-Rodriguez, D.-S. Cheong, and A. H. Heuer, Phil. Mag. **A65**, 923 (1991).
[7] U. Messerschmidt, B. Baufeld, K. J. McClellan, and A. H. Heuer, Acta Metall. et Mater. **43**, 1917 (1995).
[8] B. Baufeld, M. Bartsch, U. Messerschmidt, and D. Baither, Acta Metall. et Mater. **43**, 1925 (1995).
[9] U. Messerschmidt, B. Baufeld, and D. Baither, Plastic Deformation of Cubic Zirconia Single Crystals, to be published in: Zirconia Engineering Ceramics: Old Challenges – New Ideas, Ed. E. Kisi, Key Engineering Materials, Trans Tech Publications, Switzerland.

[10] B. Baufeld, Plastische Verformung von kubischen Zirkondioxid-Einkristallen bei Temperaturen zwischen 400 °C und 1400 °C, Thesis, Tectum Verlag, Marburg 1996, Edition Wissenschaft; Reihe Physik, Vol. 34 (Mikrofiche-Edition), ISBN 3-89608-134-91212.
[11] B. Baufeld, B. V. Petukhov, M. Bartsch, and U. Messerschmidi, to be published in Acta Mater. (1998).
[12] P. Teracher, H. Garem, and J. Rabier, in: Euroceramics, Vol. 3, Engineering Ceramics, Eds. G. deWith, R. A. Terpstra, and R. Metselaar, Elsevier Publ. Co., London 1989 (p. 3334).
[13] P. Teracher, Propriétés mécaniques de la zircone cubique monocristalline: dislocations et plasticite, Thesis, Poitiers 1990.
[14] P. Teracher, H. Garen, and J. Rabier, in: Strength of Metals and Alloys, Eds. D. G. Brandon, R. Chaim and A. Rosen, Freund Publ., London 1991 (p. 217).
[15] D. Baither, B. Baufeld, U. Messerschmidt, and M.Bartsch, Mater. Sci. Engng. A **233**, 75 (1997).
[16] J. Martinez-Fernandez, M. Jimenez-Melendo, A. Dominguez-Rodriguez, and A.H. Heuer, J. Amer. Ceram. Soc. **73**, 2452 (1990).
[17] D. Gomez-Garcia, J. Martinez-Fernandez, A. Dominguez-Rodriguez, P. Eveno, and J. Castaing, Acta Mater. **44**, 991 (1996).
[18] J. Martinez-Fernandez, M. Jimenez-Melendo, A. Dominguez-Rodriguez, and A. H. Heuer, in: Euroceramics 3, Engineering Ceramics, Eds. G. deWith, R. A. Terpstra, and R. Metselaar, Elsevier Publ. Co., London 1989 (pp. 3318 to 3322).
[19] M. Jimenez-Melendo, J. Martinez-Fernandez, A. Dominguez-Rodriguez, and J. Castaing, J. Europ. Ceram. Soc. **12**, 97 (1993).
[20] G. J. Taylor, Proc. Roy. Soc. **A145**, 362 (1934).
[21] N. H. Andersen, K. Clausen, M. A. Hackett, W. Hayes, M. T. Hutchings, J. E. MacDonald, and R. Osborn, Physica **136B**, 315 (1986).
[22] R. Osborn, N. H. Andersen, K. Clausen, M. A. Hackett, W. Hayes, M. T. Hutchings, and J. E. Macdonald, Mater. Sci. Forum **7**, 55 (1986).
[23] M. Weller, Z. Metallk. **84**, 381 (1993).
[24] M. Weller, Atomare Fehlstellen in Zirkondioxid, in: DFG-Hochleistungskeramiken, Herstellung, Aufbau, Eigenschaften, Eds. G. Petzow, J. Tobolski, and R. Telle, VCH Weinheim, 1996 (p. 413).
[25] M. Weller, private communication, 1996.
[26] M. Weller and H. Schubert, J. Amer. Ceram. Soc. **69**, 573 (1986).
[27] H. Solman, J. Chaumont, C. Dolin, and C. Monty, Ceram. Trans. **24**, 175 (1991).
[28] D. Gomez-Garcia, J. Martinez-Fernandez, A. Dominguez-Rodriguez, and K. H. Westmacott, J. Amer. Ceram. Soc. **79**, 487 (1996).
[29] D. Gomez-Garcia, J. Martinez-Fernandez, A. Dominguez-Rodriguez, and K. H. Westmacott, J. Amer. Ceram. Soc. **79**, 2733 (1996).
[30] F. R. Chien and A. H. Heuer, Phil. Mag. **A73**, 681 (1996).
[31] T. Bretheau, J. Castaing, J. Rabier, and P. Veyssiere, Adv. Phys. **28**, 835 (1979).
[32] W. R. Cannon and T. G. Langdon, J. Mater. Sci. **18**, 1 (1983).
[33] B. Burton, Phil. Mag. **A45**, 657 (1982).
[34] S. Takeuchi and A. S. Argon, J. Mater. Sci. **11**, 1542 (1976).
[35] B. Ya. Farber, A. S. Chiarelli, and A. H. Heuer, Phil. Mag. **A72**, 59 (1995).
[36] U. F. Kocks, J. Engng. Mater. Technol. **98**, 76 (1976).
[37] U. F. Kocks, Physical Basis for Non-Elastic Constitutive Relations, discussion paper at Symp. Adv. in Metal Deformation, Cornell Univ., Ithaca (NY) 1976.